Particle Accelerators, 1973, Vol. 4, pp. 129–144

EXPERIMENTAL STUDY OF THE RADIATION FIELD FROM PROTON LOSSES AROUND THE JINR SYNCHROPHASOTRON

V. YA. GVOZDEV, L. N. ZAITSEV, I. F. KOLPAKOV, A. P. KRYACHKO, N. M. NIKITYUK, AND N. I. PAVLOV

Joint Institute for Nuclear Research, Dubna, USSR

It is shown that to determine the radiation field at an accelerator operating in the beam extraction mode, the azimuthal distribution of the proton loss must be known during acceleration and extraction. Integral detectors have been used previously for measuring only the total distribution function for the proton loss from internal targets.

A system for monitoring the particle loss consisting of 20 scintillation counters, scaling, and control equipment was developed for the JINR proton synchrotron. The counters, arranged in a circular pattern near the vacuum chamber, record the flux of particles consisting primarily of protons and π mesons. After appropriate calibration it was possible to determine the absolute proton loss with a measurement error < 20 per cent.

The effect of the interceptor target for capturing secondary particles from the total distribution for the proton loss was studied to determine the location of the radiation sources. The source functions were determined from the distribution of the proton loss for different intensities and for different fractions of the extracted proton beam. These functions were used to calculate the radiation field around the proton synchrotron.

1. INTRODUCTION

The primary cause of the development of a radiation field at accelerators is the loss of protons. It is difficult to predict the radiation field for a given mode of accelerator operation and particularly difficult to predict the source distribution function, which depends on the proton loss. The term 'mode' presupposes in this case not only the accelerator adjustment but also the number, location, and effectiveness of the targets.†

The source distribution function is generally understood[1,2] to be the distribution in the chamber or the ion guide of secondary particles per centimeter that are produced as a result of the interaction of protons with the chamber walls and with the targets. The source distribution function $S_0(z)$ along the azimuth z was qualitatively analyzed in Ref. 3, in which it was written as

$$S_0(z) = S_1(z)+S_2(z)+S_3(z), \quad \text{secondary particles/cm.} \tag{1}$$

The $S_1(z)$ function denotes the distribution of the sources some distance away from the targets, and $S_2(z)$ characterizes the peaks above the targets, which are typical for any operational mode. Since both functions depend on the proton loss at the end of the acceleration cycle at constant energy E_0, we can write

$$S_m(z) = S_1(z)+S_2(z). \tag{2}$$

The function $S_3(z) = \int_0^{E_0} S_c(E_0', z)\,dE_0'$ depends upon the proton loss during acceleration, where $0 \leqq E_0' \leqq E_0$, the final energy; $S_c(E_0', z)$ is the secondary particle energy spectrum per MeV · cm.

The z integrals of the distribution functions are proportional to the proton loss.[2] For the internal targets

$$a_m L_m \gg a_c L_c,$$

where a_m and a_c are the proportionality factors and L_m and L_c are the z integrals of the given distribution functions. According to the data obtained from the integral detectors, $S_0(z)$ is assumed to be measured in a time $t_{(\text{meas})} \gg t_{(\text{cycle})}$.[2-5]

The following expression shows that for efficient beam extraction the $S_c(E_0', z)$ function must be taken into account:

$$L_0 = \bar{I}_0[(1-\eta)+\bar{\chi}], \tag{3}$$

where L_0 is the total number of lost protons per cycle, $\bar{I}_0$ is the average intensity at the end of acceleration, η is the efficiency of the beam extraction, and $\bar{\chi} = a_c L_c/a_m L_m$. For example, when $\eta = 0.95$ and $\bar{\chi} \cong 0.3$ (see Ref. 6), the radiation near the accelerator ring will depend on the proton loss during acceleration.

† By targets we mean any elements with which the beam interacts: working targets, magnets, shutters, etc.

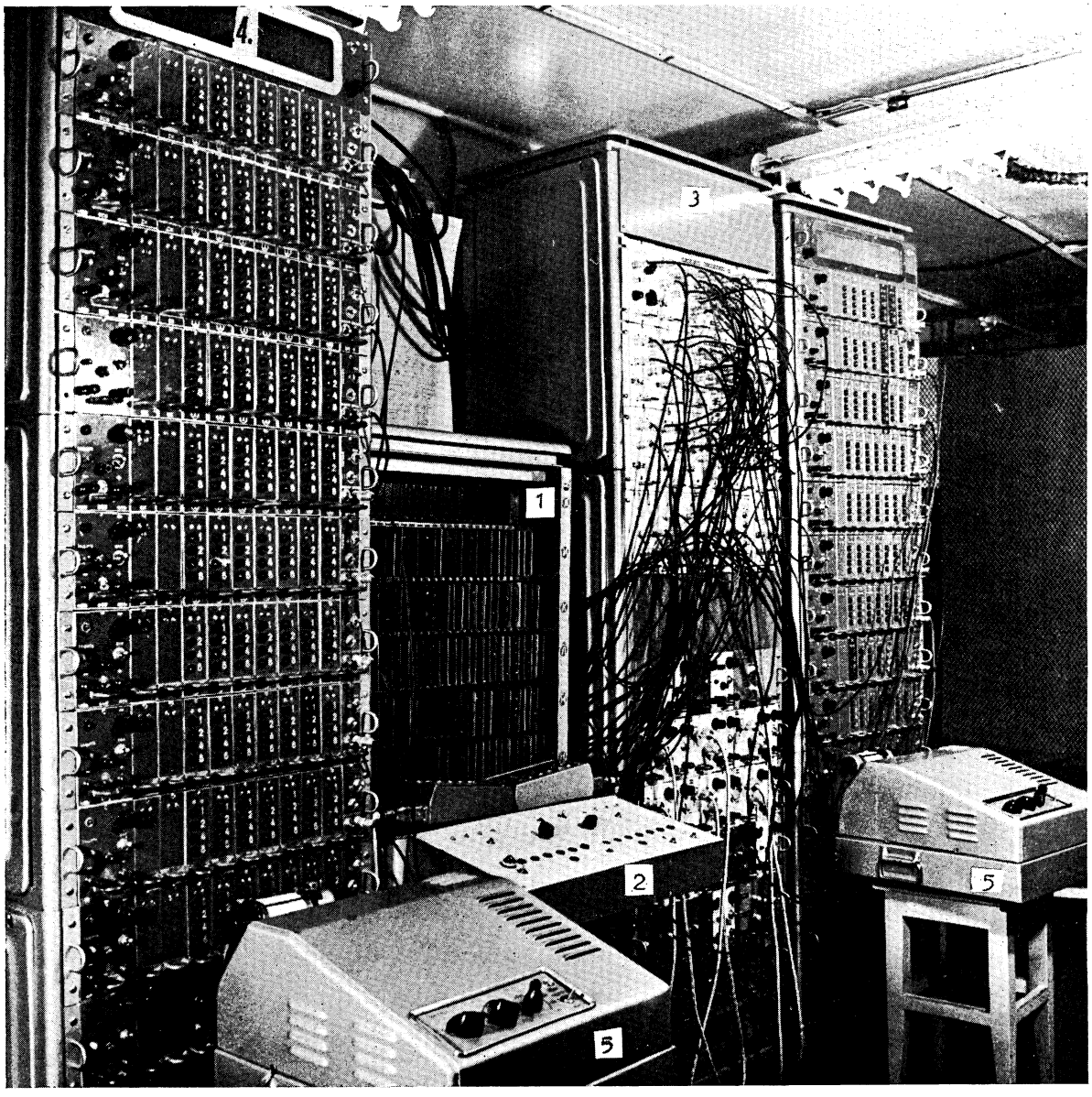

FIG. 1. Overall view of the control system and counting equipment. 1: control system based on BESM-3M computer; 2: control panel; 3: high-speed electronic equipment with high-voltage power supply (below); 4: scalers; 5: digital recorder.

Thus, for extraction of the beam all the functions appearing in Eq. (1) must be known individually. The distribution of the radiation sources $S_m(z)$ after the beam has collided with the target can be determined by the Monte Carlo method used for calculating the yield together with the spectral and angular distributions of secondary particles emitted from the target[7] and by subsequent following of the trajectories of charged particles in the magnetic field.[8,9]

A mathematical method for determining the proton loss due to the interaction of random perturbations during acceleration is more complicated and radically different from the method for calculating the proton loss at the end of the acceleration cycle. The main difficulty is that the quantitative characteristics of the perturbations for different modes of operation are known only approximately and sometimes not at all. To date, the upper limit of the perturbation based on the fraction of the proton loss attributed to it has been calculated,[10] but not the time-dependent beam layout based on the characteristics of the perturbation. The azimuthal distribution of the proton loss has not been analyzed.

We attempt in this paper to determine experimentally the distribution function $S_c(E_0', z)$ in order to establish the radiation sources for slow beam extraction and to increase the intensity of the proton synchrotron.

2. EXPERIMENTAL EQUIPMENT

Since the integral detectors are not suitable for measuring the $S_c(E_0', z)$ function, we developed a system for monitoring the particle loss during acceleration consisting of scintillation detectors, control, and counting equipment (Fig. 1). By using this system we can determine the number of secondary particles during proton acceleration for ten time intervals ranging from 10 to 300 msec.

The injection pulse with a variable delay of 200 to 2000 msec and 200 msec spacing is used as the reference point for the time intervals. The readings from all the counters along the perimeter of the accelerator are taken concurrently for the first time interval after the first cycle, for the second interval after the second cycle, etc. Multiple readings may also be taken for a single time interval after several cycles.

A block diagram of the system is shown in Fig. 2. The detectors are placed randomly around the accelerator ring. Two of them comprise a telescope, which is connected to the coincidence circuit, for monitoring the intensity $\bar{I}_0$. Signals of $\sim$0.3 V amplitude from the detectors are fed to the 2F100 shapers (0.1 V threshold) and then through the valve gates to the scalers.

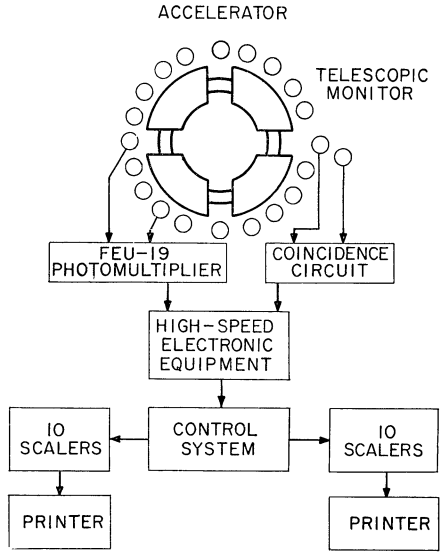

FIG. 2. Block diagram of the system for monitoring the particle loss.

The valve gates constitute a coincidence circuit, with one input lead receiving a gate pulse from the control apparatus (which determines the time intervals) and the other receiving a signal from the shaper. The signal from the telescope is conducted to one of the scalers bypassing the valve gates. The information obtained from the scalers is typed on a digital recorder's ribbons. On-line computers are used for large volumes of information.

The detectors consist of a scintillator (polystyrene with an admixture of terphenyl and POPOP), a Plexiglas light pipe, and FEU-36 photomultiplier with a divider, and a casing (Fig. 3). The scintillator (3.5 cm in diam and 2.5 cm in thickness) is covered with a 0.1 cm-thick aluminum light-proof cap. An AL-102A light diode mounted under the cap monitors the detector during accelerator shutdown.

Since the detector must be placed near the

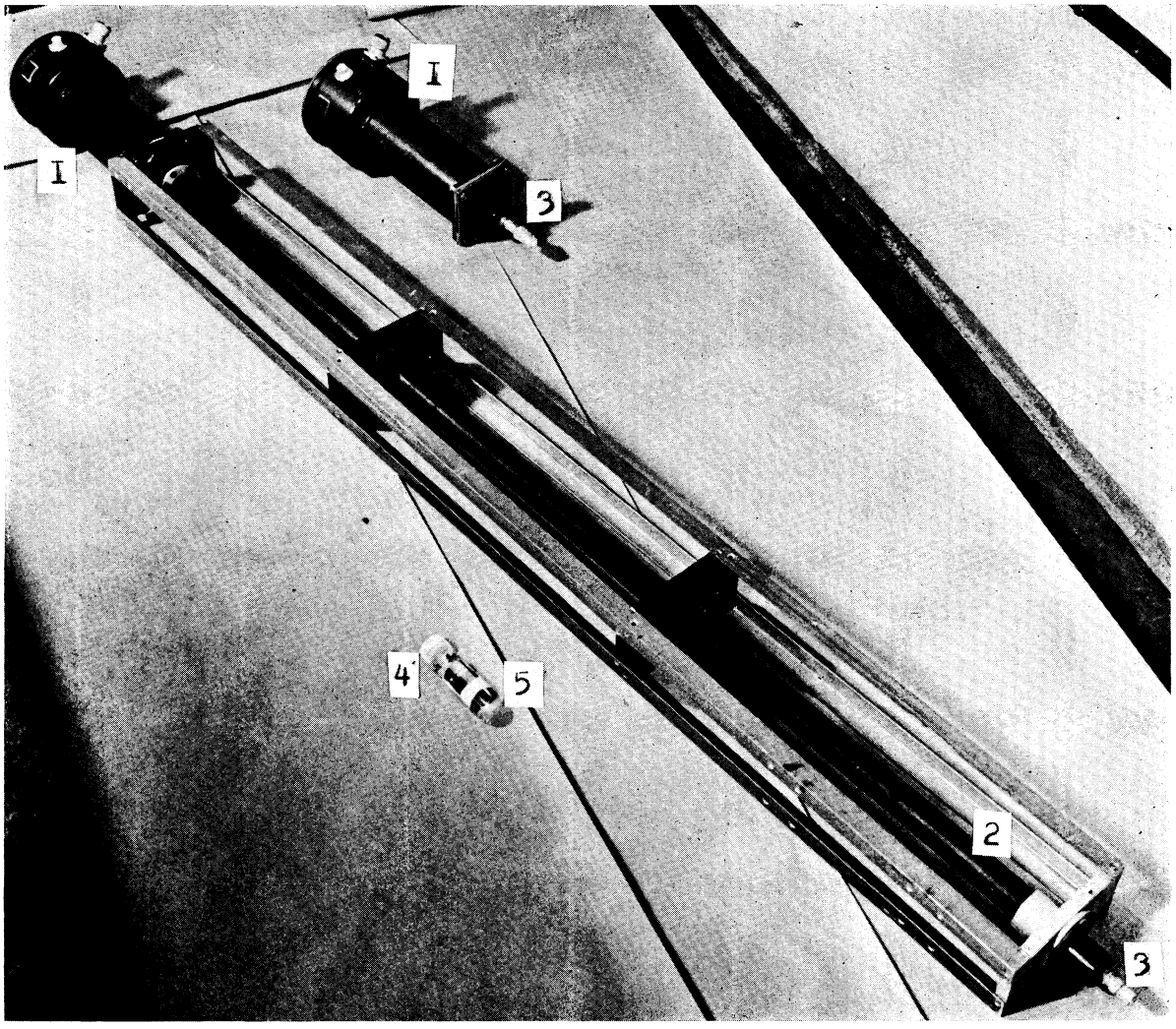

FIG. 3. Overall view of the detectors. 1: case for the FEU-36 photomultiplier with a divider; 2: 180-cm light guide; 3: cap for the scintillator and light guide; 4: scintillator 2.5 × 3.5 cm^2; 5: short 8-mm light guide.

accelerator chamber, the photomultiplier has to be located outside the strong magnetic field. A 180-cm light pipe and a photomultiplier shield consisting of three layers of steel and one layer of Permalloy ensure reliable performance of the detector in a magnetic field of 500 Oe.

3. GEOMETRY AND EXPERIMENTAL ARRANGEMENT

The arrangement of the detectors associated with the vacuum chamber of the proton synchroton is shown in Fig. 4. Four different runs (I-IV) were carried out, with 16 detectors in operation at any one time. Apart from the location of the detectors, the experimental arrangement was the same in each case.

The beam was brought to the septum magnet[3] in which it was retained at least 100 msec in a rising field. Initially it had been retained in a 12.5-kOe field, corresponding to a time of $\sim$2.8 sec after the injection pulse. A 0.3 × 0.7 × 90-cm^3 septum magnet, used as a target (without exciting windings), was placed at a distance of +28 cm from the equilibrium orbit.

A pneumatic target at distances of −10, −15, and

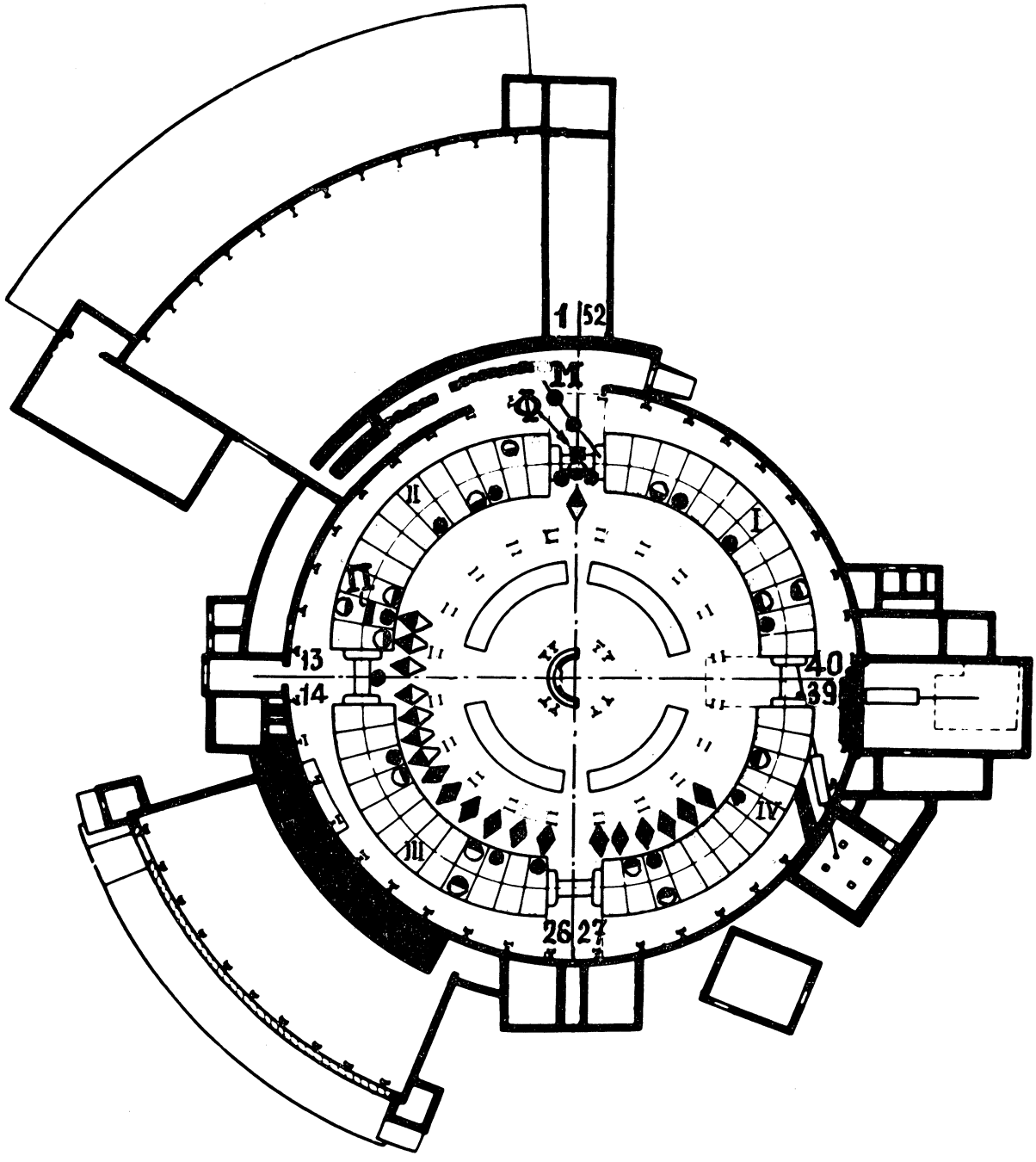

FIG. 4. Location of the detectors at the proton synchrotron. M: monitor; Φ: septum magnet; Π: interceptor target; half-filled circles: run I; filled circles: run II; filled diamonds: run III; half-filled diamonds: run IV; 1–52: sections of the ring ($\Delta z = 4$ m).

-20 cm from the equilibrium orbit was used to intercept secondary particles. The target, $10 \times 10 \times 15$ cm^3, was put into operation several microseconds before the septum magnet. Both the target and the interceptor were made of copper.

The detectors in the windows of the magnet yoke (Fig. 5) and in the straight sections admit primary protons that pass through the chamber wall without interacting (apparently at $E_0' > 1$ GeV and for angles $\alpha < 1°$), also protons undergoing elastic interaction within the wall, and secondary particles such as neutrons, charged π mesons, γ rays, positrons, electrons, and other particles produced both in the chamber walls and in the materials surrounding the detector.

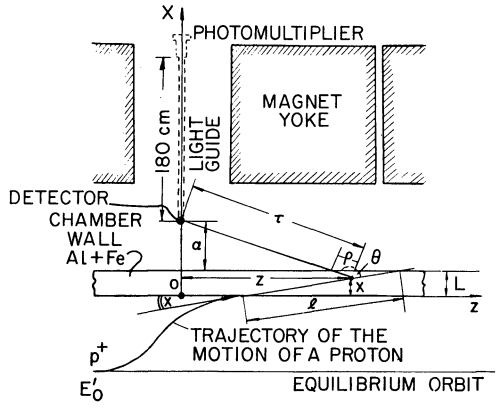

FIG. 5. Counting geometry of the spectral distribution of secondary particles at the detection point.

The types of secondary particles, their spectral and angular distributions continually change at the detection points with changing energy E_0' and magnetic field intensity. In view of this, the only estimate of the different radiation components possible is a rough one made by determining the threshold detection energy.

The threshold detection energy was determined from the positrons of the decay $^{11}C \rightarrow {}^{11}B + e^+$ resulting from the activation of carbon. If a positron from carbon decay is not detected, then the threshold energies for protons and π mesons will be 14 and 8.5 MeV, respectively. The threshold detection energies of other secondary particles were determined by taking the differences in conversion efficiency into account.

The spectra of protons, π mesons, and neutrons were calculated by assuming that a single interaction occurs between a primary proton and a nucleus. For example, the spectral distribution of protons was calculated from the following expression:

$$\frac{dN_p}{dE_p} = \frac{1-\exp\{-\int_0^l \sigma_{in}[E^k(E_0, S)]\,dS\}}{\sin\alpha} \times \int_0^L \int_{-\infty}^{+\infty} \frac{d^2N}{dE\,d\Omega} \times \exp\left\{-\int_0^{x/\sin\alpha} \sigma_{in}[E^k(E_0, S)]\,dS\right\} \times \sigma_{in}[E^k(E_0, x/\sin\alpha)] \times \exp\left\{-\int_0^{\rho} \sigma_{in}[E^k(E, S)]\,dS\right\} \times \frac{1}{\tau^2} D(x, z, E)\,dz\,dx \left[\frac{\text{secondary protons/cm}^2\ \text{MeV sec}}{\text{primary protons/cm sec}}\right], \quad (4)$$

where the geometrical notation is shown in Fig. 5 and E_0 and E are the energies of the primary and secondary protons, respectively; σ_{in} is the inelastic interaction cross section, $E^k(E^H, j)$ is the final energy of the charged particle after transmission through the thickness of the material j, i.e., $E^k = E^H - \int_0^i |dE/dt|\,dt$ (j denotes ρ, s, or $x/\sin\alpha$, respectively; E^H is the initial energy, i.e., E_0 or E, respectively); $D(x, z, E)$ is the Jacobian of the transition from the spherical coordinate system to the geometry of the experiment and from the initial energy of the particle to its energy at the measurement point. The spectral-angular distribution $d^2N/dE\,d\Omega$ was taken from Ref. 11, and the energy loss of the charged particles due to ionization dE/dt was taken from Refs. 12 and 13. Calculations were carried out in iron for $E_0 = 1, 3 \ldots, 10$ GeV (at 1-GeV intervals); $L = 1.5$ cm, d $= 40$ cm, and $\alpha = 0.02$ radian (Fig. 5). Figure 6 shows the calculated spectra for $E_0 = 3$ GeV. The shape of the neutron spectrum is compared with those of the spectra obtained in Refs. 14 and 15. For other values of E_0 the shapes of the proton, π meson, and neutron spectra are similar.

Table I gives the detection efficiency for some types of particles, from which one can readily see

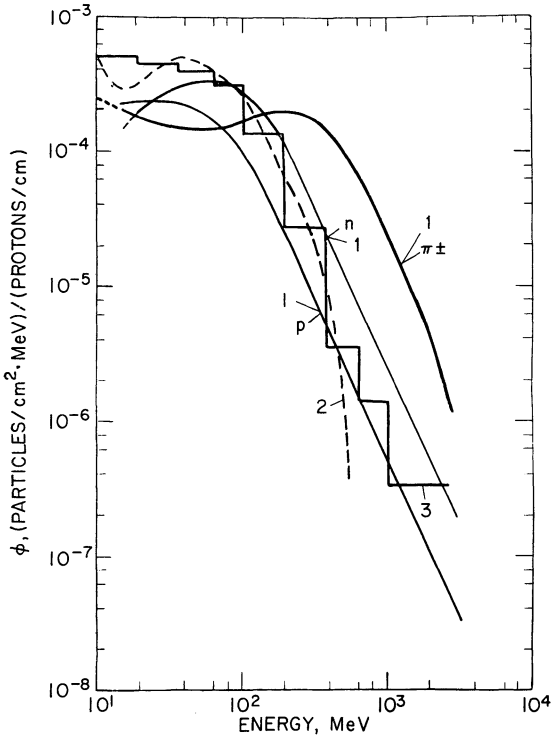

FIG. 6. Spectral distribution of protons, neutrons, and π mesons at the detection point. 1 is our calculation; see, for example, Eq. (4) for protons; 2, calculation taken from Ref. 14; 3, calculation taken from Ref. 15.

that the detectors primarily detect protons and π mesons. The detection efficiency, however, is not essential in solving the problem of interest here. The count will always be proportional to the proton loss, regardless of the type of particle detected.

TABLE I

Detection limits for some types of radiation

Type of particle (i)	E_{thresh}, MeV	Average detection efficiency, $(f_i)\%$	$\phi_i/\phi\pi$	$\frac{\phi_i f_i}{\phi_p f_p + \phi_\pi f_\pi}$
$\pi^\pm$	8.5	100	1	0.79
p	14	100	0.26	0.21
n	4	10	0.76	0.06
μ	8.5	100	~ 0	~ 0
γ	2	0.06	6.8	0.04
$\beta^\pm$	2.3	100	2×10^{-3}	1.6×10^{-3}

ϕ_i = flux density of the appropriate type of secondary particles.

However, if instead of the secondary particles, the absolute number of lost protons must be determined, then the change in the number of detected secondary particles with energy E_0' must be known.

4. ENERGY CALIBRATION

The most important stage of this work is the calibration of the system for monitoring the particle loss. The ratio of secondary particles $N(E_0')$ to that of lost protons is given by

$$N(E_0')/\alpha(E_0'), \tag{5}$$

where $\alpha(E_0')$ is the calibration constant. Calculated values for $\alpha(E_0')$ for various values of E_0' appear in Table II and are the ratios of the $(p+\pi)$ flux density at E_0' to the $(p+\pi)$ flux density at $E_0' = 1$ GeV. The flux densities of the protons and pions were obtained by integrating the calculated spectra from

TABLE II

Flux density of protons and π mesons at the detection point per single lost proton $\times$ cm^{-1} sec^{-1}

Energy range, 14 MeV to E_0', MeV $\times 10^{-3}$	Protons $\times$ cm^{-2} x sec^{-1} $\times 10^2$	Energy range, 8.5 MeV to E_0', MeV $\times 10^{-3}$	π mesons, cm^{-2} $\times$ sec^{-1} $\times$ 10	Protons $+\pi$ mesons x cm^{-2} $\times$ sec^{-1} $\times$ 10	$\alpha(E_0')$[a], Relative units
1	1.70	1	0.80	0.97	1.00
3	2.21	3	1.36	1.58	1.63
4	2.24	4	1.76	1.99	2.06
5	2.25	5	2.35	2.57	2.68
6	3.00	6	2.90	3.20	3.31
7	3.39	7	3.50	3.99	4.11
8	3.61	8	4.59	4.95	5.12
9	4.22	9	5.43	5.85	6.05
10	5.23	10	6.48	7.00	7.21

(a) $\alpha(E_0')$= (protons $\times$ π mesons) at $E_0'/0.97$.

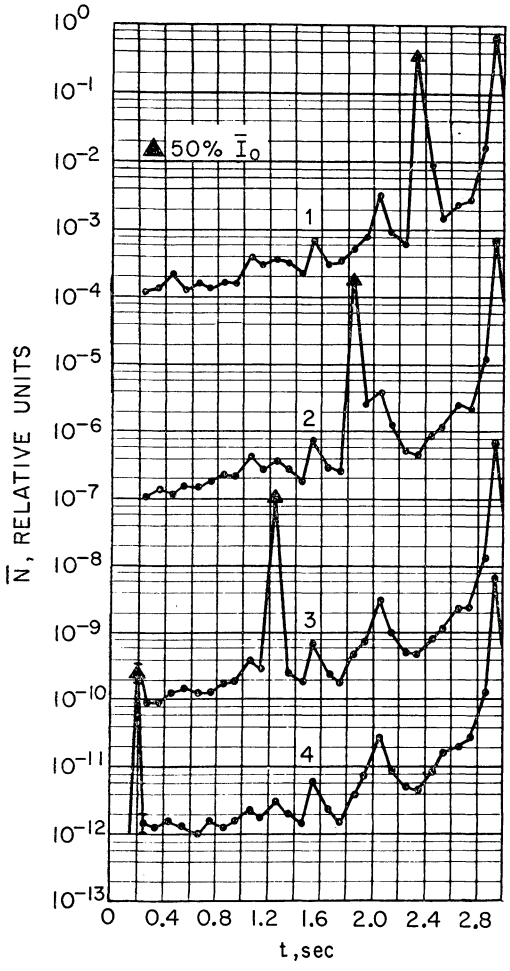

FIG. 7. $\bar{N}(t)$ function for a detector. Filled triangles indicate 50% loss of $\bar{I}_0$ after 2.3 sec (1), after 1.89 sec (2), after 1.28 sec (3), and after 0.2 sec (4).

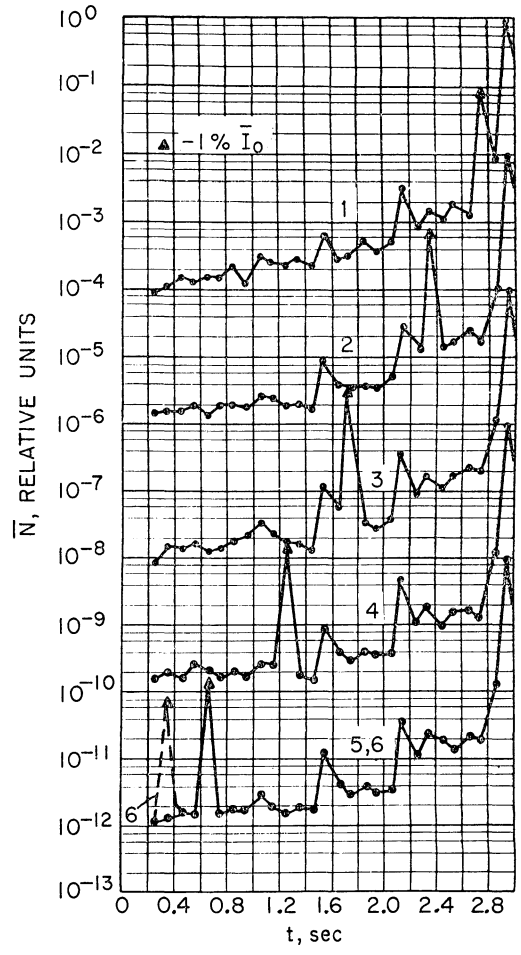

FIG. 8. $\bar{N}(t)$ function for a detector. Filled triangles indicate 1% loss of $\bar{I}_0$ after 2.75 sec (1), 2.34 sec (2), 1.7 sec (3). 1.25 sec (4), 0.7 sec (5), and 0.35 sec (6).

E_{thresh} to E_0'. Since we had only an approximate estimate of the proton and π meson spectra and since other particles could also be detected, we developed an original calibration method using the accelerator.

Single blanking pulses of 10 to 50 μsec were fed at different times up to an accelerator energy of E_0' from the generator to the accelerating voltage system. By briefly interrupting and then resuming the accelerating voltage, we changed the boundaries of the separatrix and the fraction of protons impinging on the chamber walls. The number of impinging protons, a function of the pulse time, was determined by a pickup electrode as a percentage of the average intensity $\bar{I}_0$. The time of the proton loss was recorded by all the detectors of the monitoring system.

Figures 7 and 8 show the $\bar{N}(t)$ dependences with the peaks corresponding to the given percentage loss of protons. A careful analysis of the $\bar{N}(t)$ functions for the other detectors and of the percentage loss of protons (1, 10, 30 and 50 per cent) shows that the slope of the straight lines (broken lines in Fig. 9) connecting the peaks is constant within the limits of the measurement errors. From this we determined the $\bar{\alpha}(E_0')$ dependence, which is valid for all the detectors of the monitoring system (Fig. 10).

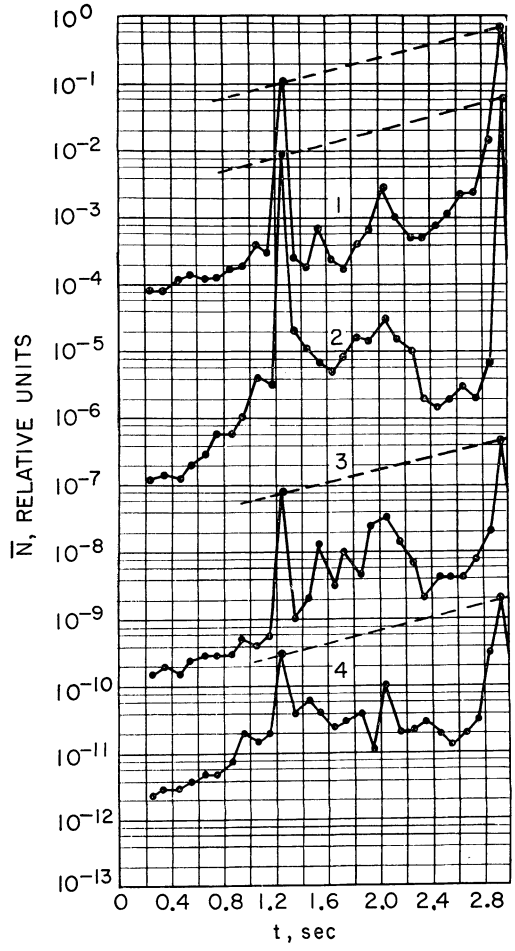

FIG. 9. $\bar{N}(E)$ function for different detectors for a 50% loss of $\bar{I}_0$. (1) detector 3 (Fig. 11); (2) detector 1; (3) detector 6; (4) detector 8.

5. AZIMUTHAL CALIBRATION

The distribution function for the proton loss along the azimuth z was determined from measurements made with several detectors. The detector readings, which varied because of the different parameters, were reduced to true values depending only on the proton loss:

$$N_i(z)/\alpha_i(z), \tag{6}$$

where $\alpha_i(z)$ is the calibration coefficient for the ith detector.

The detectors to be calibrated together with the standard were placed at a certain point on the accelerator ring. By making the detector measurements coincide with the beam descent to the septum magnet, we were able to obtain the maximum count and reduce the calibration error. Let N_{ij} be the count of the ith detector after the jth measurement and N_{kj} the count of the standard after the same measurement ($i = 1, 2, \ldots, k$ and $j = 1, 2, \ldots, n$). For convenience in analyzing the results we write the following matrix:

$$\hat{N}_{ij}\hat{\alpha}_{ikj} = \hat{N}_{kj}, \tag{7}$$

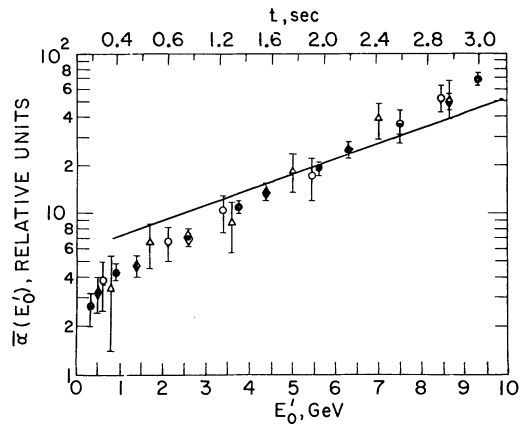

FIG. 10. Relative calibration factor $\bar{\alpha}(E_0')$ showing the data points together with a line of calculated relative values from Table II which has been adjusted to agree with the experimental data at 5 GeV.

TABLE III

$\alpha_i(z)$ Coefficients

Detector number	$\alpha_i(z)$, relative units
1	0.5743 ± 0.023
2[a]	1.0000 ± 0.020
3	0.0180 ± 0.009
4	0.3932 ± 0.020
5	0.0724 ± 0.007
6	0.5205 ± 0.031
7	0.0204 ± 0.003
8	0.0387 ± 0.005
9	0.8727 ± 0.087
10	0.4654 ± 0.065
11	0.4546 ± 0.068
12	0.0065 ± 0.002
13	0.1654 ± 0.034
14	0.0650 ± 0.010
15	0.0858 ± 0.010
16	0.0508 ± 0.009

(a) Standard

where the calibration coefficients are distributed according to the regular law with an average

$$\bar{\alpha}_{ikj} = \frac{\bar{N}_{ij}}{N_{kj}} \tag{8}$$

and with a dispersion S_α^2 for mutually correlating values.

About 10 readings were taken during the calibration, with allowance for the errors:

$$\alpha_{ik} = \bar{\alpha}_{ijk} \pm \frac{S_\alpha}{\sqrt{10}}. \tag{9}$$

Table III gives the $\alpha_i(z)$ coefficients, where i is the detector number. The azimuthal calibration was checked by comparing the distribution function $S_0(z)$ obtained from the detector measurements (run I, Fig. 4) with that from the emulsion measurements.[3] As is evident from Fig. 11, the agreement is quite satisfactory.

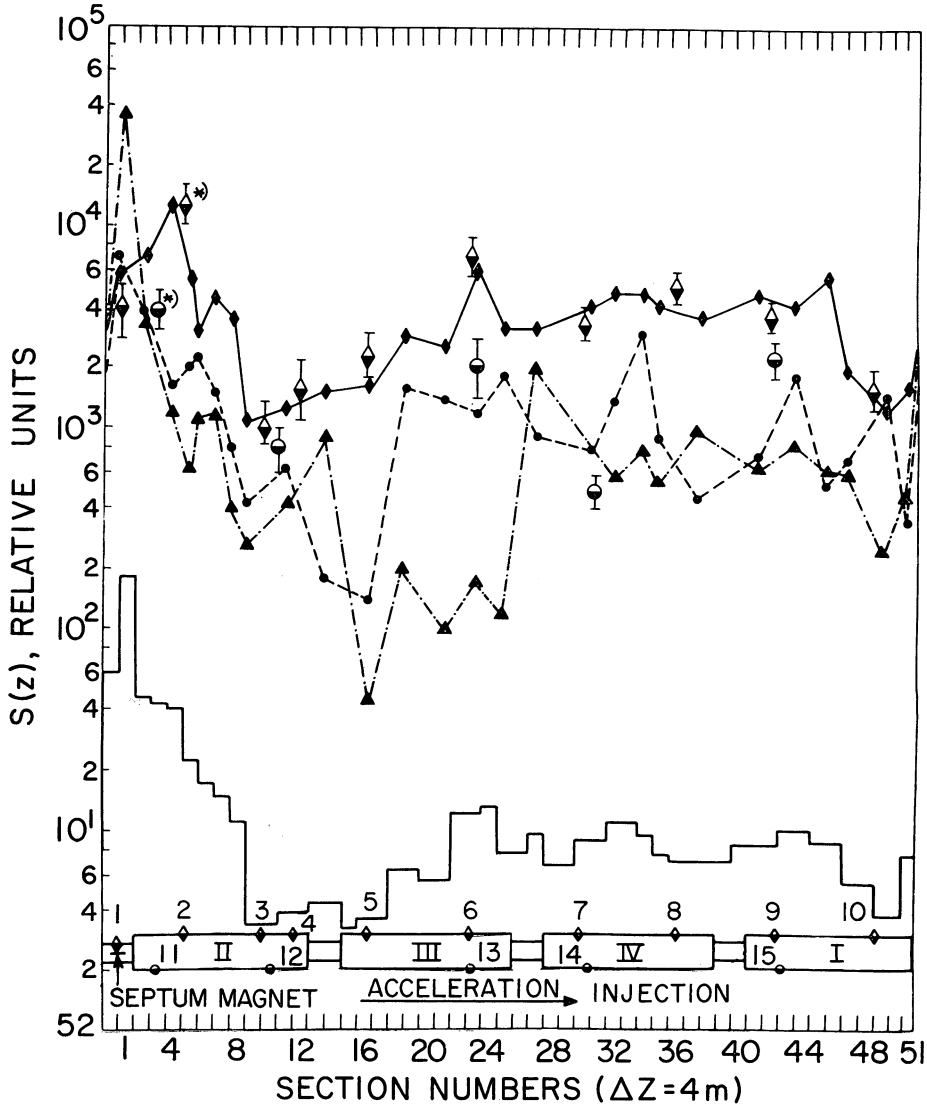

FIG. 11. Comparison of the distribution functions of secondary particles along the azimuth of the proton synchrotron. Filled diamonds: K-20 emulsion experiments on the inside chamber wall; half-filled diamonds: data obtained from the monitoring system; filled circles: K-20 emulsion measurements on the outside chamber wall; half-filled circles: data obtained from the monitoring system; filled triangles: K-20 emulsion measurements above the chamber; histogram: total distribution function[3]; *: points of intersection of the distribution functions.

6. RESULTS OF THE EXPERIMENT

The $S_c(E_0', z)$ function for $E_0' > 1$ GeV, which corresponds to $t > 400$ msec, must be known in order to determine the radiation conditions outside the proton synchrotron shield.

The average number of secondary particles is

$$\bar{N}_{ijl} = \frac{1}{n}\sum_{j=1}^{n} N_{ijl}, \qquad (10)$$

where N_{ijl} is the count from the ith detector after the jth measurement for interval number l ($i = 1, 2, \ldots, k$; $j = 1, 2, \ldots, n$; and $l = 1, 2, \ldots, m$). By taking the energy and azimuthal calibration factors into account we obtain

$$\bar{L}_{il} = \frac{\bar{N}_{ijl}}{\bar{\alpha}(E_l)\bar{\alpha}_i(z)}, \qquad (11)$$

where $\bar{\alpha}(E_l)$ was taken from the experimental data (Fig. 10) for the midpoint of the interval $\Delta E_0'$. Figure 12 shows the time-dependent (energy) distribution of the proton loss at certain points around the accelerator ring calculated according to Eq. (2).

Let us assume that the uniform distribution function for the secondary particles is located in the same region Δz as the ith detector and that the beam descent to the target always occurs during the mth time interval. We then can determine the number for the ith detector, which is proportional to the proton loss during acceleration:

$$\Delta\bar{L}_{i(c)} = a_c \sum_{l=1}^{m-1} \bar{N}_{il}. \qquad (12)$$

For all the detectors located along the azimuth this value is equal to

$$\bar{L}_c = \sum_{i=1}^{k} \Delta z_i \, \Delta\bar{L}_i. \qquad (13)$$

And for the beam descent to the target it is equal to

$$\Delta\bar{L}_{i(m)} = a_m N_{im}; \quad \bar{L}_m = \sum_{i=1}^{k} \Delta z_i \, \Delta\bar{L}_{i(m)}. \qquad (14)$$

The total integral for the proton loss is numerically equal to the intensity I_0' corresponding to time t_0 (Fig. 13):

$$a(\bar{L}_m + \bar{L}_c) = I_0'; \ (a_m = a_c = a). \qquad (15)$$

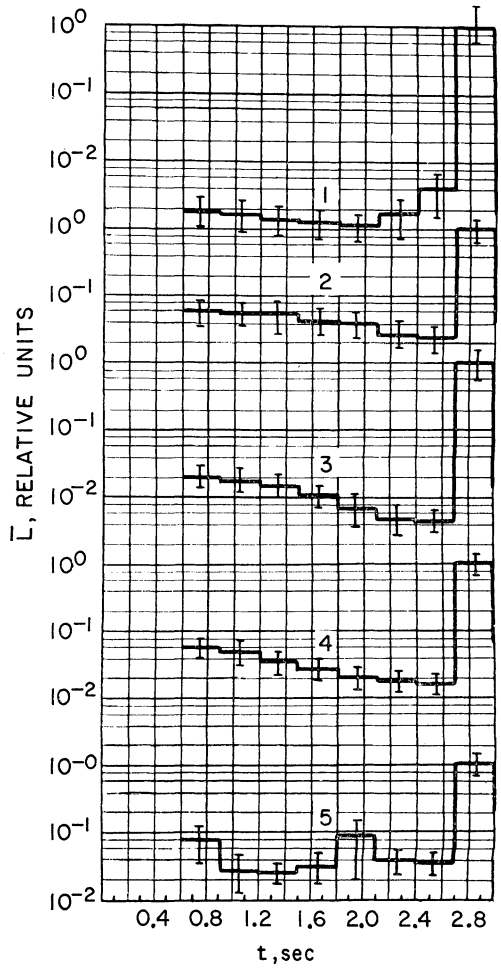

FIG. 12. Time (energy) distribution of the proton loss. (1) measured by detector 3 (Fig. 11); (2) measured by detector 1; (3) measured by detector 6; (4) measured by detector 8; (5) measured by detector 15.

Since the quantity I_0' is not known, we write Eq. (15) in terms of $\bar{I}_0$, which was monitored by the detectors,

$$a(\bar{L}_m + \bar{L}_c) = \bar{I}_0(1 + \bar{\chi}). \qquad (16)$$

The absolute proton loss (protons/cm) can be determined from the flux ϕ_i (Table II); however, for practical calculations it is sufficient to know $\bar{\chi}$ in percentage of $\bar{I}_0$.

Figure 14 shows the main results of the experiment obtained from the measurement data in runs II to IV (Fig. 4). The rms error is $\leqq$20–25 per cent. The number of secondary particles was determined in all the runs with and without the use of the

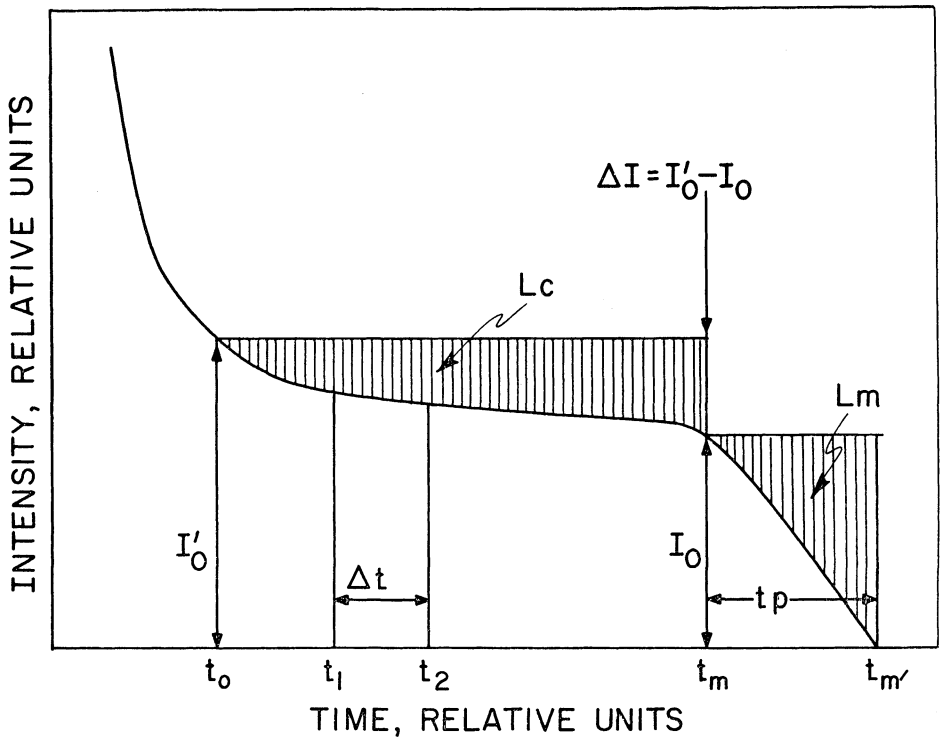

FIG. 13. Intensity of the proton synchrotron as a function of time. t_0, initial measurements by the monitoring system; $t_{m'}$ and $t_{m'}$, the initial and final descent of the beam to the septum magnet.

interceptor after the beam was brought to the septum magnet. It was established in preliminary experiments that minimum proton loss in the quiescent region occurs when the interceptor is located -10 cm from the equilibrium orbit. To compare the measurements, one of the detectors in each run was placed in the same spot near the septum magnet.

The $S_c(z)$ function was initially measured with the detectors arranged as in run II (Fig. 4). The results are presented in Fig. 14 in the form of a histogram. The distribution function was then measured in individual sections of the ring with a wider spacing of the detectors (runs III and IV). In addition, it was established that the $S_c(z)$ function remains constant at different intensities [2.2×10^9, 7.9×10^9] (stabilized), and 3.3×10^{10}. The total proton loss during acceleration $\bar{\chi}$ is 1.1, 2.2, and 12.9 per cent, respectively. The values of $\bar{\chi}$ for the first two intensities are apparently much too low, because the intensity was stabilized up to $t_0 = 0.4$ sec where $E_0' = 1$ GeV by cutting off the peripheral part of the beam cross section. This, of course, reduced the proton loss with further acceleration, as compared with the proton loss from the total beam cross section without intensity stabilization.

The source functions for different modes of operation of the proton synchroton were obtained from the results of the experiment. The following expressions were used.

$$S_0(z) = K_m S_m(z) + K_c S_c(z); \tag{17}$$

$$K_m = \bar{I}_{0m}(1-\eta)/\bar{I}_{0\,\mathrm{exp}};\ K_c = \bar{I}_{0m}\bar{\chi}_p/\bar{I}_{0\mathrm{exp}}\bar{\chi}_e \tag{18}$$

$$\int_z S_0(z)\,dz = 1. \tag{19}$$

In these equations $S_m(z)$ corresponds to Eq. (2) and $S_c(z)$ corresponds to $S_3(z)$ from Eq. (1). $\bar{I}_{0m}$ and $\bar{I}_{0\mathrm{exp}}$ are the intensities for the given mode and for the experiment respectively; $\bar{\chi}_m$ and $\bar{\chi}_{\mathrm{exp}}$ are the loss factors for the given mode and for the experiment,

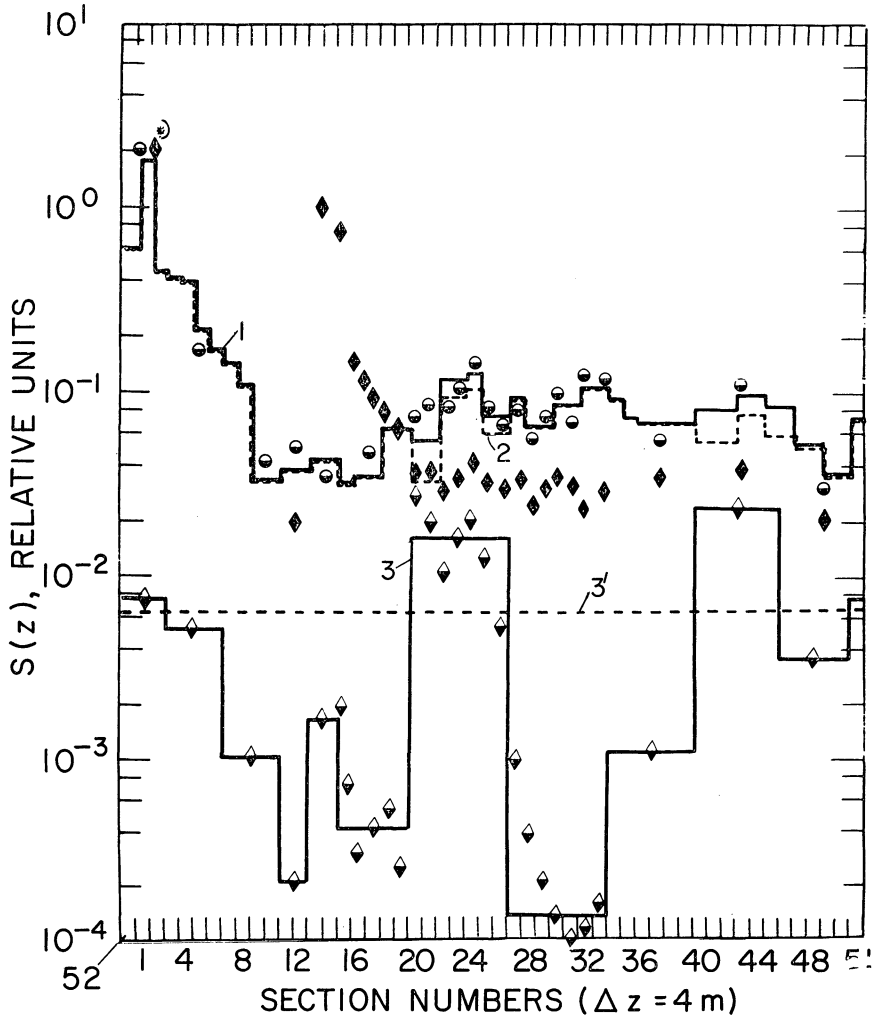

FIG. 14. Distribution functions for the loss of protons along the azimuth of the proton synchrotron. (1) total $S_0(z)$ function (see Fig. 11); half-filled circles and filled diamonds, total $S_0(z)$ function obtained from the monitoring system with and without use of the interceptor; (2) $S_m(z)$ function; (3) $S_c(z)$ function determined in run II; half-filled diamond, $S_c(z)$ function determined in runs II to IV (Fig. 4); (3′) hypothetical uniform $S_c(z)$ function; *, points of intersection of the distribution functions.

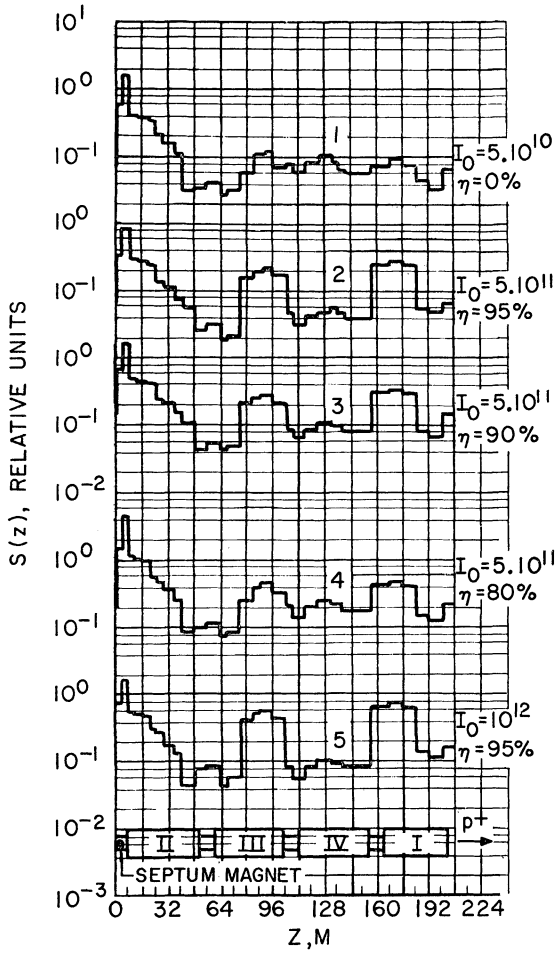

FIG. 15. Source distributions functions. (1) results of measurement (see Figs. 11 and 14); (2–5) calculations based on Eq. (17).

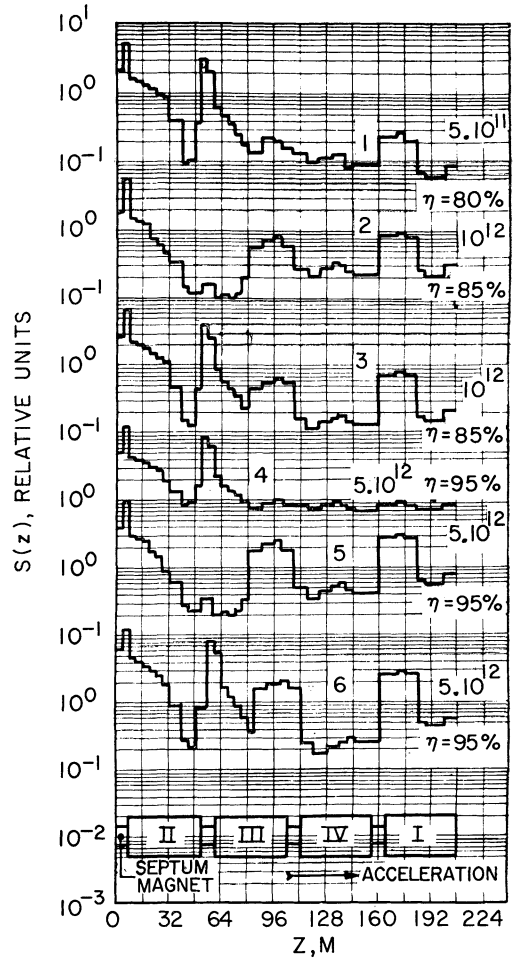

FIG. 16. Source distributions functions. (1) with use of an interceptor; (2) without use of an interceptor; (3) with use of an interceptor; (4) with use of an interceptor and a uniform $S_0(z)$ function (see Fig. 14); (5,6) with and without use of an interceptor.

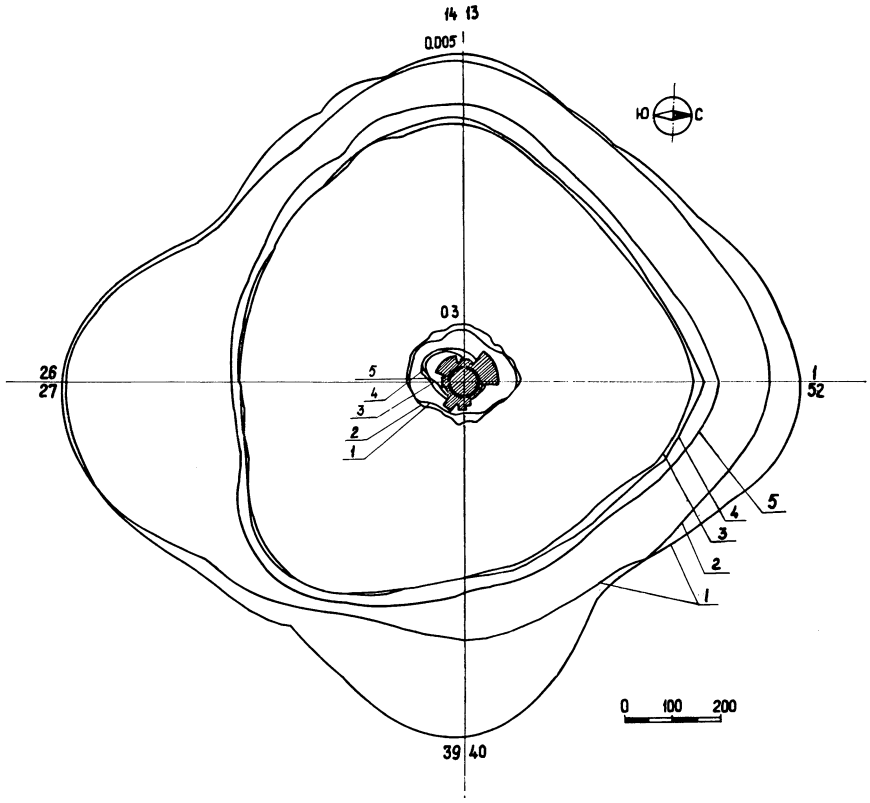

FIG. 17. Calculated isodoses (0.3 and 0.005 mrem/h) around the proton synchrotron at $E_0 = 10$ GeV, $\bar{I}_0 = 5 \times 10^{11}$ protons/cycle, and $\eta = 80\%$. (1) without use of an interceptor for $\bar{\chi} = 4\%$ (see Fig. 15, No. 4); (2) with use of an interceptor for $\bar{\chi} = 4\%$ (see Fig. 16, No. 1); (3–5) with use of an interceptor and local shielding of the septum magnet and interceptor (see Ref. 17) for $\bar{\chi} = 1$, 4, and 13%.

and η is the extraction efficiency. Figures 15 and 16 show the calculated source functions for different modes of operation of the proton synchrotron. Integral (19) was normalized to the total loss of protons $\bar{I}_{0m}(1+\bar{\chi}_m)$.

By using the method for calculating the radiation field around an accelerator described in Refs. 16 and 17, we calculated the isodose distribution around the proton synchrotron for different source functions and for the proton loss. Figure 17 is an example of one of these isodose fields. As can be seen in the figure, a change in the proton loss from 1 to 13 per cent during the acceleration cycle does not strongly affect the isodose distribution when the extraction efficiency is 80 per cent. For an intensity of 5×10^{12} and an extraction efficiency of 95 per cent, the influence of the proton loss is much stronger. On the other hand, the radiation level at the proton synchrotron can be reduced with minimum shielding cost by using an interceptor and local shielding.[18]

ACKNOWLEDGEMENTS

The authors express their gratitude to L. R. Kimel', B. S. Sychev, and I. B. Issinski for their suggestions and also to A. S. Khrykin, V. F. Tausenev, and A. L. Shishkin for their assistance in carrying out the experiments and analyzing the results.

REFERENCES

1. H. W. Patterson and R. H. Thomas, *Particle Accelerators*, **2**, 77 (1971).
2. W. S. Gilbert *et al.*, UCRL-17941, 1968.
3. L. N. Zaitsev *et al.*, JINR P16-6059, Dubna, 1971.
4. V. G. Golovachik *et al.*, IHEP, ORZ 69-114, 1969.
5. G. W. Bennett *et al.*, *Particle Accelerators*, **2**, 251 (1971).

6. Yu. M. Ado and E. A. Myae, *Atomnaya Energiya (Soviet Journal of Atomic Energy)*, **27,** 515 (1969).
7. J. Ranft, CERN MPS/Int., MU/EP, 67-5, 1967.
8. H. G. Hereward *et al.*, CERN, 65-1, 1965.
9. E. M. Kulakova *et al.*, JINR P-2880, Dubna, 1966.
10. L. L. Goldin and D. G. Koshkarev, 'Instruments and Experimental Techniques,' No. 3, 3, 1957.
11. J. Ranft, *Proc. 2nd Int. Conf. on Accelerator Dosimetry and Experience, Stanford, Nov. 5-9, 1969* (CONF-691101).
12. Do In Seb, *JETP*, **43,** 121 (1962).
13. I. K Vzorov, JINR P1-4442, Dubna, 1969.
14. K. O'Brien, HASL-240, 1969.
15. T. W. Armstrong and R. G. Alsmiller, ORNL-TM-2177, 1967.
16. L. R. Kimel' *et al.*, JINR P16-6182, Dubna, 1972.
17. L. N. Zaitsev *et al.*, JINR P16-6185, Dubna, 1972.
18. L. N. Zaitsev, *Atomnaya Energiya*, **26,** 58 (1969).

Received 13 June 1972 and in final form 10 November 1972